Bubble extinction in Hele-Shaw flow with surface tension and kinetic undercooling regularization

Dallaston, MC & McCue, SW

Original citation & hyperlink:
Dallaston, MC & McCue, SW 2013, 'Bubble extinction in Hele-Shaw flow with surface tension and kinetic undercooling regularization' *Nonlinearity*, vol 26, no. 6, pp. 1639-1665
https://dx.doi.org/10.1088/0951-7715/26/6/1639

DOI 10.1088/0951-7715/26/6/1639
ISSN 0951-7715
ESSN 1361-6544

Publisher: IOP Publishing

Bubble extinction in Hele–Shaw flow with surface tension and kinetic undercooling regularisation

Michael C Dallaston and Scott W McCue

School of Mathematical Sciences, Queensland University of Technology, Brisbane, QLD 4000, Australia

E-mail: scott.mccue@qut.edu.au

Abstract. We perform an analytic and numerical study of an inviscid contracting bubble in a two-dimensional Hele–Shaw cell, where the effects of both surface tension and kinetic undercooling on the moving bubble boundary are not neglected. In contrast to expanding bubbles, in which both boundary effects regularise the ill-posedness arising from the viscous (Saffman–Taylor) instability, we show that in contracting bubbles the two boundary effects are in competition, with surface tension stabilising the boundary, and kinetic undercooling destabilising it. This competition leads to interesting bifurcation behaviour in the asymptotic shape of the bubble in the limit it approaches extinction. In this limit, the boundary may tend to become either circular, or an infinitely thin rectangular "slit"-type shape, depending on the initial condition and the value of a nondimensional surface tension parameter. We show that over a critical range of surface tension values, both these asymptotic shapes are stable. In this regime there exists a third, unstable branch of limiting self-similar bubble shapes, with an asymptotic aspect ratio (dependent on the surface tension) between zero and one. We support our asymptotic analysis with a numerical scheme that utilises the applicability of complex variable theory to Hele–Shaw flow.

AMS classification scheme numbers: 76D27, 35B40, 35R35

1. Introduction

The Hele–Shaw cell, named after nineteenth century engineer Henry Selby Hele–Shaw, is an experimental device consisting of two parallel, closely separated plates, between which one or more fluids may be injected, flow and interact. The initial purpose of the Hele–Shaw cell was to visualise streamlines of fluid flow around objects, as the mathematical equations that govern flow in a Hele–Shaw cell (Hele–Shaw flow) are identical to those for potential (inviscid) flow [1].

Since the mid-twentieth century, there has been a wealth of study on Hele–Shaw flow problems involving free boundaries. These problems feature interfaces between different fluids in the Hele–Shaw cell whose motion is governed by the fluid flow and effects that apply to the boundary. Free boundary Hele–Shaw flow serves as a simple experimental and theoretical approximation of more complicated problems in physics and engineering

that involve moving boundaries: for instance, groundwater flow, oil recovery, melting or freezing crystals (Stefan problems), "streamers" of charged particles, and many more (see the extensive online bibliography [2], or the book [3]).

The most famous phenomenon in free boundary Hele–Shaw flow arises when one considers the interaction of fluids of differing viscosities. If the fluid of lesser viscosity displaces that with greater viscosity, the interface between them is unstable, with long fingers of the less viscous fluid developing. This is known as the Saffman–Taylor instability [4]. In particular, we imagine injecting an effectively inviscid fluid into a viscous fluid-filled Hele–Shaw cell at a point, with the inviscid fluid spreading out radially from the injection point in a highly unstable manner (see Figure 1). This is reminiscent of the formation of long thin dendrites from an initial seed in supercooled Stefan problems [5]. If the inviscid fluid is instead being removed, so that the bubble is contracting, the difference in viscosities acts to stabilise the boundary.

A valuable consequence of the simplicity of the Hele–Shaw flow equations is that many nontrivial solutions may be constructed exactly and explicitly, assuming a Bernoulli (constant pressure) condition holds on the interface [6, 7, 8]. This is achieved using complex variable methods (such as conformal mapping) to handle the evolving fluid region. For unstable problems, however, the Saffman–Taylor instability may manifest itself disastrously, with the solution "blowing up" via the interface forming infinitely sharp and fast cusps at a finite time [5, 9]. For this reason, free boundary Hele–Shaw flow with the Bernoulli boundary condition is regarded as ill-posed. To regularise the problem, additional physical effects must be included on the free boundary, which prevent the blow-up of solutions, while retaining the unstable nature of the interface. The physical effects depend on the situation being modelled. For fluid flow problems, the most natural effect to include is surface tension, which penalises high curvatures of the boundary. Many numerical and theoretical studies of the effect of surface tension in Hele–Shaw flow have been made [10, 11, 12, 13].

After surface tension, the best known regularisation is kinetic undercooling, which penalises high interfacial velocities [6]. The name comes from the use of Hele–Shaw flow as a simple model of a supercooled Stefan problem. On the moving interface between the solid and liquid phases of a freezing crystal, the temperature on the boundary is not exactly equal to the bulk melting temperature, but istead depends weakly on other surface energies which exist on the boundary. The kinetic undercooling condition comes from a relationship (often presumed linear) between the freezing temperature and the normal velocity of the interface [14]. The same condition arises in the problem of solvent penetrating into a glassy polymer [15, 16, 17]. A surface tension equivalent condition also exists in Stefan problems, due to the Gibbs–Thomson equation [18]. We also note that a kinetic undercooling equivalent condition has been used in a fluid flow context, where it can be thought of as taking into account changes in curvature of the interface in the normally ignored transverse direction [19]. It also has application to streamer discharges which precede the formation of lightning [20, 21, 22, 23].

Studies of Hele–Shaw flow or Stefan problems involving both surface tension and

kinetic undercooling regularisations are chiefly numerical (for example using level set methods [24, 25, 26]). These studies focus on the case of expanding bubbles or growing crystals; this is generally considered the more interesting problem mathematically, as it is unstable. Less attention has been paid to the case of contracting bubbles, which are generally stable. Explicit solutions for contracting bubbles exist in the absence of regularisations, and there are analytical studies into bubble breakup [27, 28, 29], the asymptotic bubble shapes (generally elliptical) [30, 31, 32, 33], and the point or points of extinction [30, 27, 31]. Additionally, there are studies on the effect of non-Newtonian fluid flow [29, 34].

To our knowledge there has been no study on the effects of surface tension and kinetic undercooling on the surface of a contracting bubble. This is remarkable, as kinetic undercooling turns out to destabilise the boundary in this normally stable direction, while surface tension remains a stabilising force. In this paper we perform an analytic and numerical study of the effect of these two boundary conditions on the shape of a single contracting bubble in Hele–Shaw flow. In particular, we determine the possible asymptotic shapes the bubble may take, and if they are stable or not. This is simpler than first appears, since for a shrinking bubble with a constant rate decrease in area, both the curvature and velocity of the interface become large as the bubble approaches a single point. This implies that it is the balance of these two forces on the boundary that determines the bubble shape, rather than the fluid flow. We show that there are two possible "trivial" asymptotic bubble shapes: the perfect circle, which is stable when surface tension dominates, and an infinitely thin rectangular "slit"-type shape, which is stable for dominant kinetic undercooling. The asymptotic bubble shapes are characterised by the limit of the aspect ratio of the bubble, with a circle having an aspect ratio of one, and the slit having an aspect ratio of zero. There exists a critical parameter range where both these bubble shapes are stable, with a third, nontrivial, unstable branch of asymptotic bubble shapes which varies over the parameters in the critical range. The limiting aspect ratio of these self-similar bubble shapes also depends on the parameters, but is always between zero and one. In this parameter range, a bubble with exactly the right initial condition could asymptote to the nontrivial shape; generally, however, a bubble ends up as either circular or slit-like, depending on its initial condition. We show that this behaviour is also observed numerically.

1.1. Formulation

The equations describing the two-dimensional Hele–Shaw problem with surface tension and kinetic undercooling are well-known [6, 35, 36, 37]. Consider a single inviscid bubble contracting at a constant rate. Let $\hat{\Omega}(\hat{t}) \subset \mathbb{R}^2$ be the region occupied by the bubble, $\partial\hat{\Omega}(\hat{t})$ be the bubble boundary, and $\hat{\phi}$ be the velocity potential of the viscous fluid outside the bubble (here we use hats to denote dimensional variables). The potential $\hat{\phi}$ is negatively proportional to the pressure inside the viscous fluid; it satisfies the problem

$$\hat{\nabla}^2\hat{\phi} = 0, \qquad (\hat{x},\hat{y}) \in \mathbb{R}^2\backslash\hat{\Omega}(\hat{t}) \tag{1}$$

$$\hat{v}_n = \frac{\partial \hat{\phi}}{\partial n}, \qquad (\hat{x}, \hat{y}) \in \partial\hat{\Omega}(t) \tag{2}$$

$$\hat{\phi} = \hat{c}\hat{v}_n + \hat{\sigma}\hat{\kappa}, \qquad (\hat{x}, \hat{y}) \in \hat{\partial}\hat{\Omega}(\hat{t}) \tag{3}$$

$$\hat{\phi} \sim -\hat{Q} \log \sqrt{\hat{x}^2 + \hat{y}^2}, \qquad (\hat{x}, \hat{y}) \to \infty, \tag{4}$$

where $\hat{c}$ is the kinetic undercooling parameter, $\hat{\sigma}$ is the surface tension parameter, $\hat{v}_n$ is the normal velocity and $\hat{\kappa}$ is the signed curvature of the interface (taken to be positive for a convex bubble). The farfield condition (4) means the bubble $\hat{\Omega}$ has a constant rate of change of area of $-2\pi\hat{Q}$; if $\hat{Q} > 0$, the bubble is contracting, while $\hat{Q} < 0$ corresponds to an expanding bubble (see Figure 1).

We reduce the number of model parameters to one by scaling lengths by $\hat{c}$ and time by $\hat{Q}/\hat{c}^2$. The resulting system is

$$\nabla^2 \phi = 0, \qquad (x, y) \in \mathbb{R}^2 \backslash \Omega(t) \tag{5}$$

$$v_n = \frac{\partial \phi}{\partial n}, \qquad (x, y) \in \partial\Omega(t) \tag{6}$$

$$\phi = v_n + \sigma\kappa, \qquad (x, y) \in \partial\Omega(t) \tag{7}$$

$$\phi \sim -\log \sqrt{x^2 + y^2}, \qquad (x, y) \to \infty, \tag{8}$$

where $\sigma = \hat{\sigma}/\hat{c}\hat{Q}$ is the nondimensional surface tension coefficient. Note that contracting bubbles now correspond to $\sigma > 0$ and t increasing, while expanding bubbles have $\sigma < 0$ and t decreasing. The nondimensional area of the bubble Ω, which we shall label $\mathcal{A}$, now has a constant rate of change given by

$$\frac{\mathrm{d}\mathcal{A}}{\mathrm{d}t} = -2\pi, \tag{9}$$

which is useful in the following analysis.

The rest of the paper is set out as follows. In Section 2 we discuss the stability of a circular interface in the nondimensionalised Hele–Shaw problem (5)–(8) with surface tension and kinetic undercooling, and show that the two effects are in competition, with the appearance of a bifurcation point $\sigma = \frac{1}{3}$ in the parameter space at which the stability of the circle changes.

In Section 3 we derive the small bubble approximation of the full Hele–Shaw problem (5)–(8), which we use to explore the behaviour of bubbles very close to extinction. In Section 4 we examine the stability of the two "trivial" steady state branches of the small bubble equation: the circle, and the infinitely thin slit-type bubble. Bubbles tending toward the slit are asymptotically rectangular, though with rounded ends (we discuss the idea of the asymptotic bubble shape more rigorously in Section 4.4). We see that there is a critical range of the surface tension $\frac{1}{3} < \sigma < \frac{1}{2}$ for which both branches are stable. In Section 5 we show that there is a nontrivial branch of steady states which separates the two trivial ones in this critical range. We observe numerically that the solutions on this branch are unstable.

In Section 6 we derive a numerical method for solving the full Hele–Shaw problem (5)–(8), which corroborates the asymptotic predictions of the previous sections. We

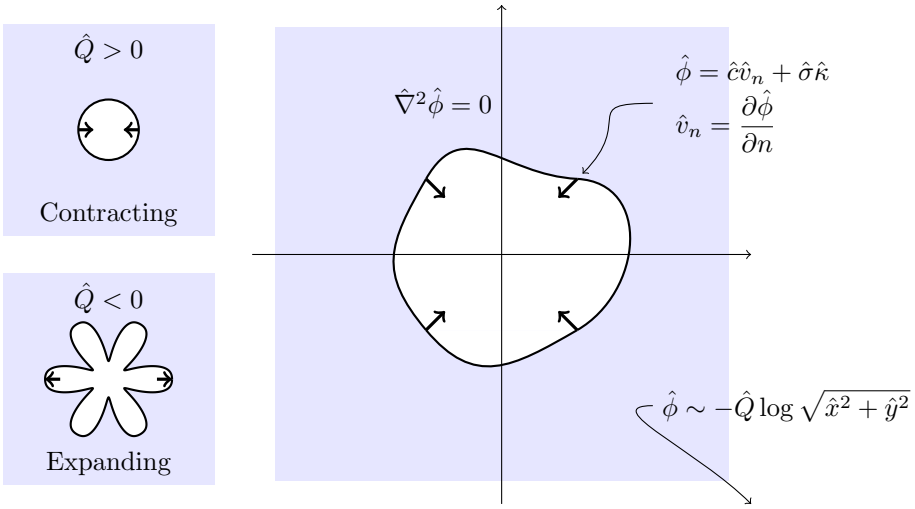

Figure 1. A schematic of the Hele–Shaw bubble problem (5)–(8). When the far-field source strength $\hat{Q}$ is positive, the bubble is contracting and the interface is generally stable. When $\hat{Q}$ is negative, the bubble expands and the interface is unstable, forming long thin fingers (the Saffman–Taylor instability). We primarily consider the contraction problem.

conclude with Section 7, which includes a discussion on possible further directions of inquiry.

2. Near-circular stability analysis

The interesting behaviour of the system (5)–(8) for contracting bubbles stems from the fact that the two nonlinear boundary effects are in competition. This can be most readily observed by examining the stability behaviour of an almost circular bubble, evolving according to the system (5)–(8). In polar (r, θ) coordinates, this system is

$$\frac{\partial^2\phi}{\partial r^2} + \frac{1}{r}\frac{\partial\phi}{\partial r} + \frac{1}{r^2}\frac{\partial^2\phi}{\partial\theta^2} = 0, \qquad s(\theta,t) < r < \infty \tag{10}$$

$$s(\phi_r - s_t) + \frac{s_\theta}{s}\phi_\theta = 0, \qquad r = s(\theta,t) \tag{11}$$

$$\phi = \frac{ss_t}{\sqrt{s^2 + s_\theta^2}} + \sigma\frac{s^2 + 2s_\theta^2 - ss_{\theta\theta}}{(s^2 + s_\theta^2)^{3/2}}, \qquad r = s(\theta,t) \tag{12}$$

$$\phi \sim -\log r, \qquad r \to \infty \tag{13}$$

where $\phi(r,\theta,t)$ is the velocity potential and $r = s(\theta,t)$ is the bubble interface $\partial\Omega$. We assume a slightly perturbed circular solution of the form

$$\phi \sim \phi_0(r,t) + \epsilon\phi_1(r,\theta,t) + \mathcal{O}(\epsilon^2),$$
$$s(\theta,t) = s_0(t) + \epsilon s_1(\theta,t) + \mathcal{O}(\epsilon^2),$$

where $\epsilon \ll 1$ (see Figure 2). To leading order in ϵ the bubble is a shrinking circle and the potential ϕ is radially symmetric:

$$\phi_0 = -\log\left(\frac{r}{s_0}\right) + \frac{\sigma - 1}{s_0}, \qquad s_0 = \sqrt{2}(t_f - t)^{1/2},$$

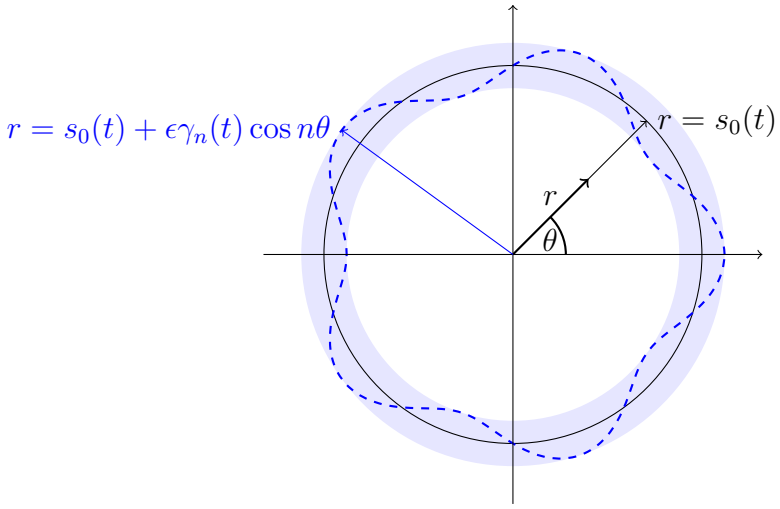

Figure 2. A schematic of the nth mode of pertutbation to a shrinking circular interface of radius $s_0(t)$. By taking the $\mathcal{O}(\epsilon)$ terms in the full Hele–Shaw problem in polar coordinates (10)–(13), we obtain a linear approximation (18) for the evolution of the nth mode $\gamma_n(t)$ as s_0 decreases.

where t_f is the extinction time. The $\mathcal{O}(\epsilon)$ problem is

$$\frac{\partial^2\phi_1}{\partial r^2} + \frac{1}{r}\frac{\partial\phi_1}{\partial r} + \frac{1}{r^2}\frac{\partial^2\phi_1}{\partial\theta^2} = 0, \qquad r > s_0(t) \tag{14}$$

$$\phi_1 \to 0, \qquad r \to \infty \tag{15}$$

$$s_{1t} = \phi_{1r} + s_1\phi_{0rr}, \qquad r = s_0(t) \tag{16}$$

$$\phi_1 + s_1\phi_{0r} = s_{1t} - \sigma\frac{s_1 + s_{1\theta\theta}}{s_0^2}, \qquad r = s_0(t). \tag{17}$$

We assume Fourier expansions for the unknown correction terms‡

$$\hat{\phi}_1 = \sum_{n=2}^{\infty} \alpha_n r^{-n}\cos(n\theta), \qquad s_1 = \sum_{n=2}^{\infty} \gamma_n\cos(n\theta).$$

Here γ_n is the nth mode of perturbation to the circle. We are interested in the stability of γ_n as the leading order radius s_0 evolves, so we define

$$\gamma_n' = \frac{\mathrm{d}\gamma_n}{\mathrm{d}s_0}.$$

Substituting into (16) and (17), and eliminating α_n, we obtain

$$\frac{\gamma_n'}{\gamma_n} = \frac{n-1}{s_0+n} + \sigma\frac{n(n^2-1)}{s_0(s_0+n)}. \tag{18}$$

This equation describes the relative rate of change of the nth mode with respect to the leading order radius s_0. Note that if

$$\frac{\gamma_n'}{\gamma_n} > \frac{s_0'}{s_0} = \frac{1}{s_0},$$

‡ We disregard the first Fourier mode ($n = 1$), as it corresponds to a translation in space (effectively moving the origin) and is therefore always neutrally stable.

then γ_n/s_0 is increasing, thus the mode is unstable for increasing s_0, and stable for decreasing s_0. The opposite holds if $\gamma_n'/\gamma_n < 1/s_0$.

2.1. Surface tension regularisation

Before considering the effect of kinetic undercooling, we revise the effect of surface tension on the contracting bubble, where kinetic undercooling is absent ($\hat{\sigma} \geq 0$, $\hat{c} = 0$). In this case, the dynamic condition (12) becomes

$$\phi = \sigma \frac{s^2 + 2s_\theta^2 - s s_{\theta\theta}}{(s^2 + s_\theta^2)^{3/2}}. \tag{19}$$

This changes the equation for stability of the nth mode (18) so that

$$\frac{\gamma_n'}{\gamma_n} = \frac{n-1}{s_0} + \sigma \frac{n(n^2-1)}{s_0^2}.$$

For the unregularised system ($\sigma = 0$) where the bubble is contracting (s_0 decreasing), the second mode is neutrally stable, and all other modes are stable. This is consistent with known elliptical extinction behaviour, for which exact solutions exist [6, 29, 30, 31]. For contraction with nonzero surface tension ($\sigma > 0$),

$$\frac{\gamma_n'}{\gamma_n} = \frac{n-1}{s_0} + \sigma \frac{n(n^2-1)}{s_0^2}$$

which is greater than $1/s_0$ for all $n \geq 2$, thus even the second mode decays, leading to a circle in the extinction limit. For expanding problems, the source strength at infinity $\hat{Q} < 0$, and therefore $\sigma \leq 0$, and s_0 is increasing. In this case the interface is, in general, unstable. However, for $\sigma < 0$, we have

$$\frac{\gamma_n'}{\gamma_n} < \frac{1}{s_0} \quad \text{when} \quad -\sigma > \frac{n-2}{n(n^2-1)} s_0 \sim \frac{s_0}{n^2} \ (n \to \infty).$$

Thus surface tension has the effect of stabilising the high order modes when the bubble is expanding. Indeed, since

$$\max_{n \geq 2} \frac{n-2}{n(n^2-1)} = \frac{1}{24} \qquad (\text{the } n = 3 \text{ case}),$$

all modes (and therefore the interface) are stable when s_0 is less than the critical radius $s_0^* = 24(-\sigma)$. This summary is similar to the stability analysis in Paterson [38].

2.2. Kinetic undercooling

The stability properties of the problem with purely kinetic undercooling ($\hat{\sigma} = 0, \hat{c} > 0$) are very different. In this case, (18) becomes

$$\frac{\gamma_n'}{\gamma_n} = \frac{n-1}{s_0 + n}.$$

This equation holds regardless of the sign of $\hat{Q}$, due to the invariance of the kinetic undercooling problem under change of clock (which also implies the problem is time-reversible [6, 37]). Any mode that is stable for the contracting bubble is necessarily unstable for the expanding bubble, and vice-versa. In particular, we have

$$\frac{\gamma_n'}{\gamma_n} > \frac{1}{s_0} \quad \text{when} \quad s_0 > \frac{n}{n-2}.$$

This implies that for contracting bubbles (s_0 decreasing), the second mode γ_2 is always unstable, and each higher mode becomes successively unstable as s_0 decreases below $n/(n-2)$, until $s_0^* = 1$ at which time all modes become unstable. Conversely, for expanding bubbles, all modes are stable for $s_0 < 1$, then become unstable, starting with the high modes. Unlike surface tension, kinetic undercooling does not stabilise the high modes, although it does moderate their instability. A similar property is also observed in the stability analysis of a planar front in a channel geometry [6, 37]. We do not consider the case of pure kinetic undercooling further in the bulk of this paper (however, see the discussion in Section 7).

2.3. Surface tension and kinetic undercooling

Considering (18) for both nonzero surface tension and kinetic undercooling, for the nth mode to be stable as the bubble contracts we require

$$s_0 > \frac{n}{n-2} - \sigma\frac{n(n^2-1)}{n-2}. \tag{20}$$

Thus surface tension decreases the critical radius at which the nth mode becomes unstable due to kinetic undercooling. Indeed, if $\sigma > 1/(n^2-1)$, then the nth mode is stable for all time. This implies there is a value of the surface tension, $\sigma = \frac{1}{3}$, at which all modes are stable except the second, which is neutrally stable. This value of σ is a bifurcation point, where the stability of bubbles changes. We explore the issue of stability further in the following sections, by analysing the behaviour of bubbles very close to extinction.

2.4. Higher mode instabilities

The above result (20) implies that the second mode γ_2 is the most unstable. For this reason we focus our attention on symmetric elliptic or oval-shaped bubbles. We do not consider in depth the case where the second mode is exactly zero, for instance if the bubble initially has an n-fold symmetry (where $n > 2$). In this case the value of the surface tension at which the stability of the circle changes is given by

$$\sigma_{cn} = \frac{1}{n_{\min}^2 - 1}, \tag{21}$$

(where $n_{\min}$ is the smallest n with nonzero mode γ_n). The possible non-circular extinction shapes will also be different; see the discussion in Section 7.

3. The small bubble asymptotic limit $t_f - t \ll 1$

Once a bubble evolving according to the system (5)–(8) has contracted to a small size, the leading order problem becomes significantly simpler, as we see below. Here we assume the bubble does not break into multiple disconnected bubbles, but approaches a single extinction point (see the discussion in Section 7). Solutions to this "small bubble" problem allow us to analyse the behaviour of the full system near extinction. The simplification arises from the fact that the curvature and velocity terms in the dynamic condition (7) become large as the bubble area goes to zero, so it is the balance of terms in this equation that determine the bubble shape, rather than the potential flow in the fluid region.

For simplicity we assume a bubble symmetric in the x- and y-axes. The nondimensional dynamic condition (7) in Cartesian (x, y) coordinates is

$$\phi = \frac{f_t}{\sqrt{1+f_x^2}} - \sigma \frac{f_{xx}}{(1+f_x^2)^{3/2}}, \qquad y = f(x,t), \tag{22}$$

where $y = f(x,t)$ represents the bubble boundary $\partial\Omega$, which we may consider in the first quadrant ($x, y \geq 0$). Let $x = \lambda(t)$ be the x-intercept of the bubble ($f(\lambda(t), t) = 0$), and define scaled space variables $x = \lambda X$ and $y = \lambda Y$. The free surface is represented by the function $Y = F(X,T) = f(x,t)/\lambda$, where

$$T = -\log \lambda$$

is the new time-like variable§. Since $\lambda \to 0^+$ as the bubble approaches its extinction point, this substitution stretches time such that $T \to \infty$ as $t \to t_f^-$ (the extinction time). It is clear that the curvature term in (22) is $\mathcal{O}(\lambda^{-1})$. Additionally, we have

$$f_t = \dot{\lambda}(F - XF_X - F_T),$$

and, using the constant change of area (9),

$$\frac{\mathrm{d}\mathcal{A}}{\mathrm{d}t} = \frac{\mathrm{d}}{\mathrm{d}t}\left(4\lambda^2 \int_0^1 F(X,T)\,\mathrm{d}X\right) = -2\pi,$$

which implies

$$\dot{\lambda} = -\frac{\pi}{2\lambda}\left(\int_0^1 2F - F_T\,\mathrm{d}X\right)^{-1},$$

so the velocity term in (22) is also $\mathcal{O}(\lambda^{-1})$. Now considering the pressure term in (22), if we write

$$\phi \sim \frac{1}{\lambda}\Phi_0 + \mathcal{O}(1), \qquad y = f(x,t),$$

the leading order term Φ_0 must be spatially uniform, as all other effects are $\mathcal{O}(1)$. Consequently, the $\mathcal{O}(1/\lambda)$ approximation of (22) is

$$P(T) = \frac{F - XF_X - F_T}{\sqrt{1+F_X^2}} + S(T)\frac{F_{XX}}{(1+F_X^2)^{3/2}}, \tag{23}$$

§ This choice of scaling is the only one for which we see time dependence at leading order in small λ.

with boundary conditions $F(1,T)=0$, $F_X(0,T)=0$, where

$$S(T)=\frac{2\sigma}{\pi}\int_0^1 2F-F_T\,\mathrm{d}X. \tag{24}$$

The scaled pressure term $P(T)=\Phi_0/(\lambda\dot{\lambda})$ is fixed by the constant change of area (9). In our rescaled formulation, it is determined by multiplying (23) by $\sqrt{1+F_X^2}$ and integrating. This is equivalent to integrating (7) over $\partial\Omega$ with respect to arclength. The result is

$$P(T)=(1-\sigma)\frac{\int_0^1 2F-F_T\,\mathrm{d}X}{\int_0^1\sqrt{1+F_X^2}\,\mathrm{d}X}. \tag{25}$$

Any numerical and asymptotic analysis of (23) is hampered by the fact that we require F to have a square root singularity at $X=1$, so that the bubble does not have a corner on the x-axis. The singularity is removed by making the substitution $\xi=\sqrt{1-X^2}$, which results in the problem

$$P(T)=\frac{\xi F+(1-\xi^2)F_\xi-\xi F_T}{\sqrt{\xi^2+(1-\xi^2)F_\xi^2}}+S(T)\frac{\xi(1-\xi^2)F_{\xi\xi}-F_\xi}{(\xi^2+(1-\xi^2)F_\xi^2)^{3/2}}, \tag{26}$$

where $F=F(\xi,T)$, with the single remaining boundary condition $F(0,T)=0$. We will dedicate the majority of this paper to the analysis of this equation to inform us of the extinction behaviour of bubbles in the original Hele–Shaw problem (5)–(8). Note that F now has the correct square root behaviour as $X\to 1$ (or $\xi\to 0$) as long as $F_\xi(0)>0$. While it seems that (26) is underdetermined, in fact the equation is singular at both end points (since the coefficient of the highest derivative vanishes at $\xi=0$ and $\xi=1$), while the one boundary condition provides an alternative to (25) for determining the value of P. Indeed, setting $\xi=0$ in (26) results in

$$P(T)=1-\frac{S(T)}{F_\xi(0,T)^2}. \tag{27}$$

3.1. Relation to curve-shortening flow

The small bubble approximation (23) implies that, in the small bubble limit, the evolution of the bubble shape with surface tension and kinetic undercooling boundary conditions is determined by the balance between the normal velocity and curvature of the interface. It should come as no surprise then that this problem is related to curve-shortening flow, in which the normal velocity and curvature are equal: $v_n=-\kappa$, for our convention on the sign of the curvature (see [39, 40, 41], for instance). Indeed, any solution to (23) that tends to a circle is also tending to a solution to curve-shortening flow, as v_n and $-\kappa$ both tend to -1. As with (9), the bubble area under curve-shortening flow decreases at constant rate -2π.

Additionally, our small bubble problem (26) is equivalent to curve-shortening flow for a special value of the surface tension, $\sigma=1$. Under the same assumptions of

symmetry and rescaling we used to obtain (23), the equation for curve shortening flow is

$$0 = \frac{F - XF_X - F_T}{\sqrt{1+F_X^2}} + S(T)\frac{F_{XX}}{(1+F_X^2)^{3/2}}, \tag{28}$$

where

$$S(T) = \frac{2}{\pi}\int_0^1 2F - F_T \,\mathrm{d}X. \tag{29}$$

It is clear that (28) and (29) are equivalent to (23) and (24) for $\sigma = 1$ (note that (25) implies $P = 0$ in this case). Thus, for this particular value of σ, the abundance of theory that exists for curve-shortening flow holds for our problem as well. Grayson's theorem states that bubbles of any initial shape contract under curve-shortening flow to a bubble which is asymptotically circular in the extinction limit [39]. This is consistent with the circle being stable according to our analysis in Section 4 for the relevant value $\sigma = 1$. Additionally, in curve-shortening flow there is the exact "paperclip" solution (or "Angenent oval") that demonstrates the evolution of an initially oval bubble to a circle [40, 41]. Thus the paperclip also represents an exact solution to (23) when $\sigma = 1$. It is an open question as to whether there are any nontrivial explicit solutions to (23)-(24) for $\sigma \neq 1$.

3.2. Numerical solution

To verify the asymptotic results in the following sections, it is useful to solve the small bubble problem (26) numerically. To achieve this goal, we discretise F at evenly spaced node points ξ_j by $F(\xi_j, T) = F_j(T)$, and use central finite difference approximations for the derivatives in (26), replacing the left hand side with (27). We compute the integral (24) using the trapezoid rule. Satisfying (26) at each node point (including the end points, at which we find the derivatives by extrapolation) provides a system of fully implicit ordinary differential equations for the unknowns F_j, which are advanced in time using the fully implicit method `ode15i` implemented in `Matlab`. In testing this code, we found well-behaved solutions for relatively few (50-100) nodes, which runs in the order of seconds on a modern desktop computer.

4. Stability of the circle and the slit steady states

4.1. Steady states of the small bubble problem

The possible asymptotic shapes of contracting bubbles in the full system (5)–(8) in the limit $t \to t_f^-$ correspond to the steady states of the small bubble approximation (26) as $T \to \infty$. In general, the existence and stability of steady states depends on the surface tension parameter σ. By inspection, $F = \xi$ is a steady state for any σ; it represents the perfect circle (recall $\xi = \sqrt{1-X^2}$). The contracting circle is also an exact solution of the full problem (5)–(8); in Section 2 we showed that it is stable for $\sigma > \frac{1}{3}$ and unstable

for $\sigma < \frac{1}{3}$. In the current section we show this is also true of the small bubble problem (26).

Additionally, we may consider $F = 0$ a steady state of (26) for all σ, although this solution violates the requirement on the boundary that $F_\xi(0) > 0$. This steady state, a line on the x-axis with infinitely sharp ends, represents a bubble which asymptotically takes a "slit"-type shape (that is, whose aspect ratio goes to zero, rather than remaining $\mathcal{O}(1)$, in the extinction limit). We discuss the concept of the asymptotic shape of a shrinking bubble in Section 4.4.

Because the steady state itself violates the boundary condition at $\xi = 0$, the standard eigenvalue analysis for stability is not applicable. Instead, we consider the slit to be stable or unstable depending on whether the aspect ratio of near-slit bubbles (with small aspect ratio but rounded ends) increases or decreases in T. The determination of this stability involves solving a boundary layer problem near the ends of the bubble. In the current section we show this steady state bifurcates at a different value of σ than the circle; the slit is stable for $\sigma < \frac{1}{2}$ and unstable for $\sigma > \frac{1}{2}$. The overlapping interval $\frac{1}{3} < \sigma < \frac{1}{2}$, in which both "trivial" steady states are stable, suggests that there is a third, unstable branch of steady states in this interval. We consider this nontrivial branch in Section 5.

4.2. The circular bubble

To test the linear stability of the circular bubble, represented by $F_0(\xi) = \xi$, we perturb the circle by writing

$$F(\xi, T) = \xi + \epsilon F_1(\xi, T), \qquad \epsilon \ll 1,$$

and expand (26) in small ϵ, keeping terms to order ϵ. The result is a linear equation for F_1:

$$2\sigma F_{1\xi}(0) = \xi F_1 - \xi F_{1T} + \sigma\xi(1-\xi^2)F_{1\xi\xi} + \sigma(2-3\xi^2)F_{1\xi}.$$

Recall that no boundary conditions are required, as the problem is singular at both end points. Performing separation of variables $F = \mathcal{T}(T)G(\xi)$, we find that $\mathcal{T} = \exp(\mu T)$ and G satisfies the ordinary differential equation:

$$2\sigma G'(0) = \xi(1-\mu)G + \sigma\xi(1-\xi^2)G'' + \sigma(2-3\xi^2)G', \tag{30}$$

where μ is an eigenvalue. From the equation for $\mathcal{T}$, the bubble will be linearly stable if all $\Re\{\mu\}$ are less than zero, and unstable if at least one is greater than zero.

We remove dependence of (30) on the surface tension σ by writing the eigenvalues as $\Lambda = (1-\mu)/\sigma$, and remove the nonlocal term on the left hand side by defining a new dependent variable $H(\xi)$ by

$$G = \frac{1}{\xi}\left(H + \frac{2G'(0)}{\Lambda+1}\right).$$

The equation (30) now reduces to a more familiar singular Sturm–Liouville form:

$$(1-\xi^2)H'' - \xi H' + (\Lambda+1)H = 0, \qquad H'(0) = 0.$$

Indeed, this is a Chebyshev differential equation whose eigenfunctions are the Chebyshev polynomials

$$H_k(\xi) = \cos(\sqrt{1+\Lambda_k}\sin^{-1}\xi),$$

and for H_k to be real and differentiable at $\xi = 1$ we require $\sqrt{1+\Lambda_k} = 2k$ for positive integers k (we may exclude $k = 0$ as it corresponds to constant H, which is equivalent to the trivial solution $G = 0$). Putting the eigenvalue back in terms of μ we have

$$\mu_k = 1 - \sigma(4k^2 - 1),$$

thus the largest eigenvalue is $\mu_1 = 1 - 3\sigma$, which is positive for $\sigma < 1/3$ and negative for $\sigma > 1/3$. Thus the stability of the circle in the small bubble problem (26) is identical to that seen in the full problem (5)–(8). This result is to be expected; indeed, we obtain Chebyshev eigenfunctions in Cartesian coordinates as they are the equivalent to the Fourier modes in polar coordinates used in Section 2 for the full problem.

4.3. The thin slit

To examine the stability of the thin slit steady state, we assume $F = \mathcal{O}(\epsilon)$, where $\epsilon \ll 1$, and expand the unknowns in small ϵ:

$$F \sim \epsilon F_1, \qquad P \sim \epsilon P_1, \qquad S \sim \epsilon S_1, \qquad \epsilon \to 0.$$

To $\mathcal{O}(\epsilon)$, the problem (26) reduces to the first order equation

$$P_1 = F_1 - F_{1T} + \frac{1-\xi^2}{\xi}F_{1\xi}, \qquad F_1(0,T) = 0.$$

Note that the reduction in order from a second order to a first order equation suggests that the asymptotic limit is singular; in particular, the boundary condition at $\xi = 0$ cannot be satisfied, so we expect there to be a boundary layer near $\xi = 0$ where the balance of terms in (26) is different.

First we consider the outer problem ($\xi = \mathcal{O}(1)$). If we define $\alpha_1(T) = F_1(1,T)$, so that $\alpha = \epsilon\alpha_1$ is the time-dependent aspect ratio, then setting $\xi = 1$ implies $P_1 = \alpha_1 - \alpha_1'$. Letting $G = F_1 - \alpha_1$, so that $G(1,T) = 0$, we obtain a truly local first order partial differential equation for G:

$$G_T - \frac{1-\xi^2}{\xi}G_\xi = G, \qquad G(1,T) = 0, \tag{31}$$

whose solution is obtained by the method of characteristics. For some initial condition $G(\xi,0) = G_0(\xi)$ on $\xi \in [0,1]$, the solution is

$$G(\xi,T) = G_0\Big(\sqrt{1+(\xi^2-1)\mathrm{e}^{-2T}}\Big)\,\mathrm{e}^T. \tag{32}$$

As $T \to \infty$, the characteristics carry the zero boundary condition in (31) across the entire interval; thus $G \to 0$, and F tends to α_1. In particular,

$$F_1(0,T) = \alpha_1(T) + G_0(\sqrt{1-\mathrm{e}^{-2T}})\mathrm{e}^T \to \alpha_1(T), \qquad T \to \infty.$$

The thin bubble will be stable or unstable depending on whether α_1 is decreasing or increasing. To determine the stability we must analyse the inner problem. For simplicity,

we may assume that enough time has passed such that $F_1(0,T)$ may be taken to be α_1, in which case α_1 becomes the far field condition for the inner problem inside the boundary layer near $\xi = 0$.

We now consider the inner problem. The balance of terms in (26) changes when $\xi = \mathcal{O}(\sqrt{\epsilon})$, giving the characteristic width of the boundary layer. Let

$$\xi = \sqrt{\epsilon}\eta, \qquad F \sim \epsilon F_1(\eta), \qquad \epsilon \to 0,$$

so that (26) becomes, to leading order,

$$0 = F_{1\eta}^{(\mathrm{I})}(\eta^2 + F_{1\eta}^{(\mathrm{I})2}) + S_1(\eta F_{1\eta\eta}^{(\mathrm{I})} - F_{1\eta}^{(\mathrm{I})}), \tag{33}$$

with $F_1^{(\mathrm{I})}(0) = 0$ and $F_1^{(\mathrm{I})}(\eta,T) \to F_1(0,T)$ as $\eta \to \infty$ (here we use $F_1^{(\mathrm{I})}$ to distinguish the inner solution from the outer solution)‖. The far field condition provides the matching between the inner and outer solutions. This is a first order Bernoulli equation in $F_{1\eta}^{(\mathrm{I})}$ that is linearised by the substitution $G = (F_{1\eta}^{(\mathrm{I})})^{-2}$. The resulting solution is

$$F_1^{(\mathrm{I})} = S_1 \cos^{-1}\left[k_1 \exp\left(-\frac{\eta^2}{2S_1}\right)\right] + k_2, \tag{34}$$

where k_1 and k_2 are arbitrary constants. The boundary conditions imply

$$k_2 = -\cos^{-1}\left(\frac{k_1}{S_1}\right), \qquad k_2 = F_1(0,T) - S_1\frac{\pi}{2}.$$

However, since

$$F_{1\eta}^{(\mathrm{I})} = \frac{\eta}{\sqrt{k_1^2 \exp\left(\frac{\eta^2}{S_1}\right) - 1}},$$

and we need $F_{1\eta}^{(\mathrm{I})} \neq 0$ for the bubble to behave properly (with a square root singularity) near $X = 1$, we require $k_1 = 1$. Solving for k_2 and S_1 simultaneously, we find

$$k_2 = 0, \qquad S_1 = \frac{2}{\pi}F_1(0,T) \sim \frac{2\alpha_1(T)}{\pi}, \qquad T \to \infty.$$

The definition of S (24) implies

$$S_1 = \frac{2\sigma}{\pi}(2F_1(1) - F_T(1)) = \frac{2\sigma}{\pi}(2\alpha_1 - \alpha_1'),$$

thus we obtain an equation for α_1

$$\alpha_1'(T) \sim \left(2 - \frac{1}{\sigma}\right)\alpha_1(T), \qquad T \to \infty. \tag{35}$$

Therefore the thin slit steady state is stable for $\sigma < \frac{1}{2}$ and unstable for $\sigma > \frac{1}{2}$. Furthermore, for $\sigma < \frac{1}{2}$, the asymptotic shape of the bubbles is given by (34). Substituting the known values for S_1, k_2 and k_3, and putting in terms of F and X, (34) becomes

$$F(X,T) \sim \frac{2\alpha(T)}{\pi}\cos^{-1}\left[\exp\left(-\frac{\pi(1-X^2)}{4\alpha(T)}\right)\right], \qquad T \to \infty. \tag{36}$$

‖ Note that the time derivative disappears when we take the leading order inner problem. Thus for a given initial condition, there is also a time boundary layer problem in which the solution in the inner ξ region rapidly evolves to (34). However, we do not examine this complication in any greater detail.

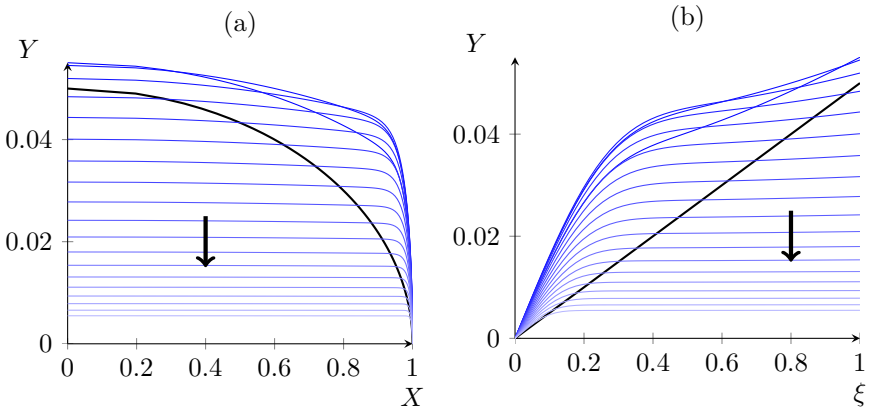

Figure 3. The numerical solution of the bubble evolution equation (26) in (a) X and (b) ξ, for $\sigma = 0.4$. The bubble is initially a thin ellipse of aspect ratio $\alpha(0) = 0.05$ (denoted by the thick solid line). The numerical solution quickly develops a boundary layer with inner solution (near $X = 1$, or $\xi = 0$) predicted in (34), while the outer solution tends to a time dependent constant which decays as predicted by (35).

The aspect ratio $\alpha = \epsilon\alpha_1$ decays exponentially, according to (35):

$$\alpha(T) \sim A\mathrm{e}^{(2-1/\sigma)T}, \qquad T \to \infty, \tag{37}$$

where A is a constant depending on the initial bubble shape. To verify out asymptotic predictions, in Figure 3 we show a representative numerical solution of (26) for an initially thin elliptical bubble with surface tension $\sigma = 0.4$. At this value we expect the slit to be stable, and the numerical solution confirms this result. As predicted by our asymptotic analysis, the bubble interface quickly develops an inner boundary layer, which looks like (34). As time progresses, the outer solution tends to a time-dependent constant, as predicted by (32). The asymptotic bubble shape is then given by (36), which evolves according to (37).

4.4. The asymptotic shape of the thin bubble

Previously we refer to the thin bubble described by (36) as asymptotically a rectangle with rounded ends. Here we define the idea of an asymptotic bubble shape more rigorously. As the bubble boundary approaches a point in (x, y) coordinates as $\lambda \to 0$, to define an asymptotic bubble shape we must perform a dynamic (time-dependent) rescaling of space such that the bubble approaches a shape in the limit. For bubbles whose aspect ratio tends to a nonzero constant, this is achieved simply through the scaling with respect to λ that we perform in Section 3.

For the bubble described asymptotically by (36), where the aspect ratio $\alpha(T) \to 0$ as $T \to \infty$, a limiting shape is not achieved by scaling x and y by the same time-dependent parameter. Instead, we could consider scaling such that the x and y intercepts always map to unity; that is, take $X = x/\lambda$ as before, and define $\tilde{Y} = Y/\alpha = y/(\lambda\alpha)$. Under such a scaling, the solution (36) approaches the unit square in the $(X, \tilde{Y})$ as $T \to \infty$ (see Figure 4). In this sense, we say the thin bubbles are asymptotically rectangular.

However, this scaling does not capture the shape of the bubble near the tip, since this behaviour occurs only in the boundary layer near $X = 1$, which shrinks as $\alpha \to 0$ (by symmetry, the same situation occurs near $X = -1$). To observe the asymptotic tip shape, we must scale both spatial coordinates by the same amount. To this end, we rescale by $\tilde{X} = (X-1)/\alpha$, with $\tilde{Y} = Y/\alpha$ as before. To leading order in α, (36) becomes

$$\tilde{Y} \sim \frac{2}{\pi} \cos^{-1} \left[\exp\left(\frac{\pi \tilde{X}}{2} \right) \right]. \tag{38}$$

This equation describes the "rounding off" of the rectangular bubble, and is also depicted in Figure 4. The equation for the bubble shape (38) can be rearranged to be

$$\frac{\tilde{X}}{2} = \frac{1-l}{\pi} \log \left[\frac{1}{2} \left(1 + \cos \frac{\pi(\tilde{Y}/2)}{l} \right) \right], \qquad l = \frac{1}{2}. \tag{39}$$

The curve represented by (39) is equivalent to the shape of the famous Saffman–Taylor finger for width $l = \frac{1}{2}$ (see Equation 17 of [4]), and is also known as the "grim reaper": an exact solution in curvature-driven flow [40, 41] and the shape of a viscous filament in a Hele–Shaw channel. [42]. Indeed, if we examine (23) near the tip of a thin bubble, using the expansions

$$F \sim \epsilon F_1, \qquad P \sim \epsilon P_1, \qquad S \sim \epsilon S_1, \qquad X = \epsilon \tilde{X} - 1,$$

for $\epsilon \ll 1$, then we obtain the leading order problem (equivalent to (33))

$$-\frac{1}{S_1} \frac{F_{1\tilde{X}}}{\sqrt{1 + F_{1\tilde{X}}^2}} = \frac{F_{1\tilde{X}\tilde{X}}}{(1 + F_{1\tilde{X}}^2)^{3/2}},$$

which is a scaled travelling-wave version of the equation ($v_n = -\kappa$) for curve-shortening flow, with a wave speed of $-1/S_1$. As the grim reaper is the travelling wave solution of the curvature driven flow problem [40, 41], it occurs in the thin-bubble limit of our problem also. The overall bubble shape is reminiscent of a scaled and time-reversed version of the "paperclip" solution to curve-shortening flow [40, 41] for time $t \to -\infty$, though the two shapes are likely only the same in the limits $t \to -\infty$ and $T \to \infty$.

5. The nontrivial branch of steady states

In this section we show that there is a third branch of steady states of (26) which exists only when the surface tension lies in the critical range $\frac{1}{3} < \sigma < \frac{1}{2}$. For each σ in this range there is a nontrivial steady state with aspect ratio α. This branch of steady states approaches the circle steady state as $\sigma \to \frac{1}{3}^+$ (with $\alpha \to 1^-$) and approaches the slit steady state as $\sigma \to \frac{1}{2}^-$ ($\alpha \to 0^+$). We numerically compute the bubble shapes and the relation between α and σ. Additionally we obtain the asymptotic form of the bubble shape as $\alpha \to 0^+$. Since this steady state separates the circle and the slit, which are stable for $\frac{1}{3} < \sigma < \frac{1}{2}$, we expect it to be unstable. We provide numerical evidence to support this prediction.

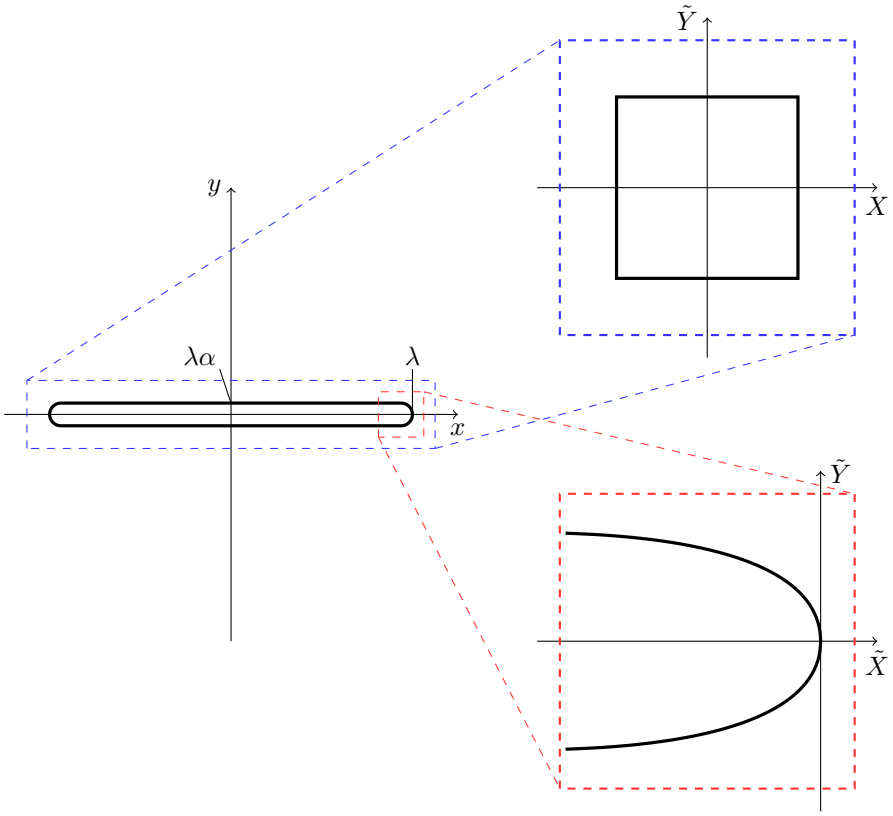

Figure 4. A schematic of the description of the asymptotic shape of the thin bubble, represented by the solution (36), under different scalings. If we scale by $X = x/\lambda$ and $\tilde{Y} = y/(\lambda\alpha)$, such that the intercepts are at unity, the bubble is asymptotically square. This does not capture the behaviour at the tips of the bubble, however. By zooming in near the tip using the new horizontal scaling $\tilde{X} = y/(\lambda\alpha)$, we observe the rounded-off asymptotic limiting shape of the end of the bubble (38). This tip shape is equivalent to the Saffman–Taylor finger and the travelling wave solution in curvature-driven flow, known as the grim reaper (see Section 4.4).

5.1. Numerical computation

To determine this nontrivial branch of steady states, we take the steady state version of (26):

$$P = \frac{\xi F + (1-\xi^2)F'}{\sqrt{\xi^2 + (1-\xi^2)F'^2}} + S\frac{\xi(1-\xi^2)F'' - F'}{(\xi^2 + (1-\xi^2)F'^2)^{3/2}}, \tag{40}$$

with $F(0) = 0$, P an undetermined constant, and where $'$ represents differentiation with respect to ξ. Instead of using σ as an input, we will instead fix the aspect ratio $\alpha = F(1)$ between 0 and 1 and let S be an unknown which must be found as part of the solution. The value of σ is then deduced from S. As before, (40) is a singular boundary value problem, for which we expect well-determined solutions as the two boundary conditions may be used to find the two unknowns P and S.

We solve (40) numerically by discretising with central finite difference approximations for the derivatives. The unknowns are P, S, and the values of F at

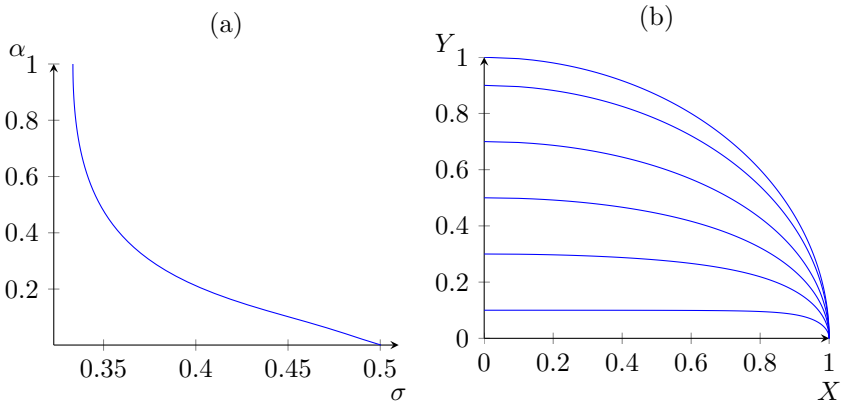

Figure 5. (a) The aspect ratio of the numerical solution of (40) against the corresponding value of surface tension σ. This represents the nontrivial, unstable branch of steady states which separates the circle and slit steady states, which are both stable in the critical range $1/3 < \sigma < 1/2$. (b) Some representative solutions on this nontrivial branch.

interior points, while the system of equations comes from the discretisation of (40) at the interior and both end points. The numerical value of σ is then computed from S using the steady state version of (24):

$$S = \frac{4\sigma}{\pi} \int_0^1 \frac{\xi F}{\sqrt{1-\xi^2}} \, \mathrm{d}\xi. \tag{41}$$

This process is carried out for a range of values α between 0 and 1. The resulting curve of α against σ is shown in Figure 5, along with some representative bubble shapes for various α. Note in particular that as $\alpha \to 1^-$, $\sigma \to \frac{1}{3}^+$ and the bubble shape approaches a circle. That is, this nontrivial branch of solutions intersects the branch of circular steady states at the bifurcation point (the point where the stability of the circle steady state changes). Conversely, as $\alpha \to 0^+$, $\sigma \to \frac{1}{2}^-$, the bifurcation point of the slit steady states.

5.2. The thin bubble limit

In addition to the numerical solution we look at the thin bubble limit of steady states on the nontrivial branch by considering (40) with aspect ratio $\alpha \ll 1$. This is very similar to the boundary layer problem we solved for the stability of near-slit bubbles in Section 4. Expanding the unknowns,

$$F \sim \alpha F_1, \qquad P \sim \alpha P_1, \qquad S \sim \alpha S_1,$$

the leading order problem is

$$P_1 = F_1 + \frac{1-\xi^2}{\xi} F_1', \qquad F_1(0) = 0, \; F_1(1) = 1,$$

which has solution $F_1 = P_1 + k_1\sqrt{1-\xi^2}$ where k_1 is arbitrary. To avoid a singularity at $\xi = 1$, we must have $k_1 = 0$ and so $F_1 = P_1 = 1$.

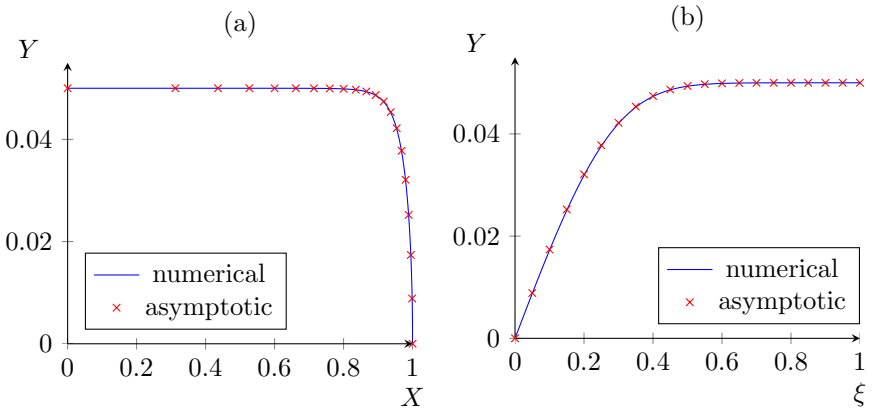

Figure 6. A comparison between the thin bubble asymptotic approximation (43) and the numerical solution to (40) for a bubble on the nontrivial solution branch, (a) in physical coordinate X and (b) in transformed coordinate ξ. The aspect ratio is set to $\alpha = 0.05$, small enough that the asymptotic approximation is very good.

This solution cannot be made to satisfy the condition at $\xi = 0$, so we expect there to be a boundary layer at this end. The balance of terms in (40) changes when $\xi = \mathcal{O}(\sqrt{\alpha})$. Let

$$\xi = \sqrt{\alpha}\eta, \qquad F \sim \alpha F_1(\eta),$$

so that (40) becomes, to leading order,

$$0 = F_1'(\eta^2 + F_1'^2) + S_1(\eta F_1'' - F_1'), \qquad F_1(0) = 0, \ \lim_{\eta\to\infty} F_1 = 1, \tag{42}$$

(where $'$ is now differentiation with respect to η). This is identical to the inner problem (33) for the stability of a near-slit bubble. An exact solution to (42) is easily found and the requirement $F'(0) > 0$ again determines the value of S_1:

$$F_1 = \frac{2}{\pi}\cos^{-1}\left[\exp\left(-\frac{\pi\eta^2}{4}\right)\right], \qquad S_1 = \frac{2}{\pi}.$$

Thus the asymptotic bubble shape in terms of X is

$$F \sim \alpha\frac{2}{\pi}\cos^{-1}\left[\exp\left(-\frac{\pi(1-X^2)}{4\alpha}\right)\right], \qquad \alpha \to 0. \tag{43}$$

A comparison between (43) and the numerical solution to (40) for small α is shown in Figure 6. Since the integral in (41) $\sim \alpha$, we can also determine the value σ from S_1:

$$\sigma = \frac{1}{2}.$$

This is the result predicted by the numerical scheme, and is the bifurcation point for the stability of the slit steady state. The bubbles shapes on the nontrivial branch are asymptotically described by (43) as the aspect ratio $\alpha \to 0^+$. In this limit, the bubbles look like long thin rectangles with rounded ends (as described in Section 4.4), similar to the stable near-slit evolving bubbles (36) which do not lie on the nontrivial branch.

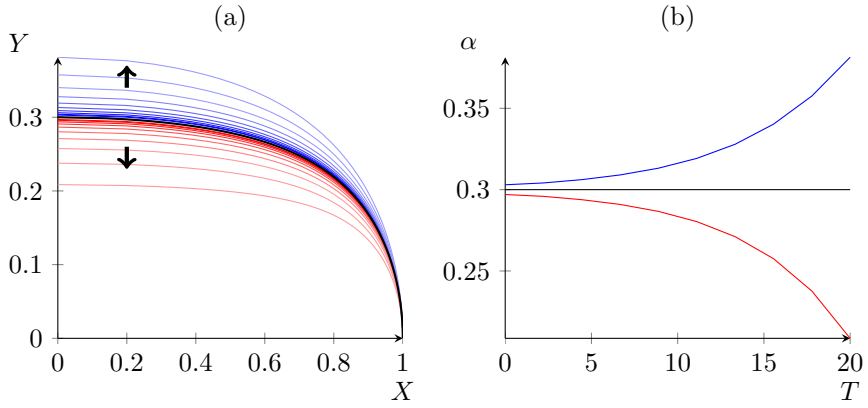

Figure 7. A numerical demonstration of the instability of the nontrivial steady state solution of (26) for surface tension $\sigma = 0.3757$, corresponding to steady state aspect ratio of 0.3. In (a), a solution which is initially at the steady state (the thick solid curve) remains there. Additionally, two solutions are shown that are initially slightly above and below the steady state. These solutions head away toward the trivial (stable) circle and slit steady states, respectively. In (b) we plot the aspect ratios of the three solutions over time.

5.3. Stability

The linear stability problem for the nontrivial branch of steady states is more difficult than that for the two trivial steady states, and we do not attempt an analysis here (see the discussion in Section 7, however). We demonstrate the instability numerically by solving (26) using the method discussed in Section 3.2, with an initial condition equal to the numerically computed nontrivial steady state for the given value of σ, multiplied by a constant slightly greater than, equal to, or less than unity. The result is shown in Figure 7, with the two solutions that are not exactly at the steady state initially heading away towards either of the stable trivial steady states.

5.4. Bifurcation diagram

We are now at a point where we may summarise the steady state behaviour of the small bubble problem (26), and therefore the asymptotic near-extinction behaviour of the full Hele–Shaw problem (5)–(8). This is most easily done with a bifurcation diagram, which is shown in Figure 8. The steady states of (26) are readily identified by their aspect ratios α, which we plot against the surface tension parameter σ. The diagram also indicates the bifurcations in the stability of the two trivial steady states (the circle and slit), and in the critical region $\frac{1}{3} < \sigma < \frac{1}{2}$, where both trivial steady states are stable, we include the numerically computed nontrivial branch.

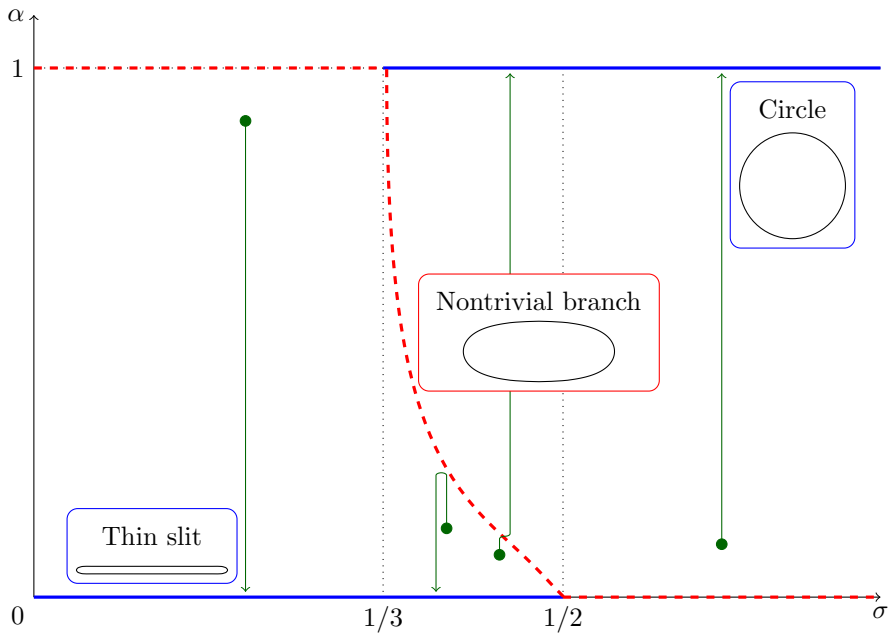

Figure 8. A bifurcation diagram for the small bubble problem (26) which summarises the main results of Sections 4 and 5. The aspect ratios α of possible steady states are plotted against the parameter σ. For $\sigma > \frac{1}{2}$ and $\sigma < \frac{1}{3}$, only the two trivial steady states exist, with the circle ($\alpha = 1$) and the slit ($\alpha = 0$) stable in the respective ranges. For the critical range $\frac{1}{3} < \sigma < \frac{1}{2}$, both trivial steady states are stable, with a third, unstable steady state (computed from (40)) separating them. Also included are typical trajectories for solutions to either the small bubble problem (26) or the full Hele–Shaw problem (5)–(8).

6. Numerical solution to the full Hele–Shaw problem

To show that the steady state behaviour of the small bubble problem (26) does indeed represent the asymptotic behaviour of the full Hele–Shaw problem (5)–(8), a numerical solution to this full problem is required.

Our numerical scheme is based on applying a spectral collocation-type scheme to a complex variable formulation of the problem. Complex variable methods are used extensively in constructing exact solutions in unregularised Hele–Shaw problems [6] and have also been used to devise numerical methods similar to the one we present here [36]. Our numerical scheme has two variants; an unscaled version which is purely based on the full problem (5)–(8), and an adaptation that takes advantage of the scaling we used in finding the small bubble problem in Section 3.

6.1. Unscaled method

Let $z = g(\zeta, t)$ be an analytic, time-dependent mapping function under which the fluid region $z \in \Omega(t)$ is the image of the unit disc (g will be analytic in the unit disc except at $\zeta = 0$, where it has a simple pole corresponding to infinity in the z-plane). The

kinematic condition may be written as a boundary condition for g on the unit circle:

$$\Re\{g_t\overline{\zeta g_\zeta}\} = \Re(\zeta\Phi_\zeta) = 1 - \Re\{\zeta V_\zeta\} - \sigma\Re\{\zeta K_\zeta\}, \qquad |\zeta| = 1, \tag{44}$$

where $\Phi = \phi + \mathrm{i}\psi$ is the complex velocity potential, and V and K are complex analytic functions in the unit disc whose real boundary data is the normal velocity and curvature respectively, that is

$$\Re\{V\} = v_n = \frac{\Re\{g_t\overline{\zeta g_\zeta}\}}{|\zeta g_\zeta|}, \qquad \Re\{K\} = \kappa = \frac{\Re\{\zeta(\zeta g_\zeta)_\zeta\overline{\zeta g_\zeta}\}}{|\zeta g_\zeta|^3},$$

on $|\zeta| = 1$. For simplicity we assume a bubble symmetric in the x and y-axes. The mapping function g (and its derivatives) may therefore be written as a power series with time-dependent coefficients:

$$g(\zeta,t) \;= \sum_{n=0}^{\infty} a_n(t)\zeta^{2n-1}, \quad \zeta g_\zeta = \sum_{n=0}^{\infty}(2n-1)a_n(t)\zeta^{2n-1},$$
$$\zeta(\zeta g_\zeta)_\zeta = \sum_{n=0}^{\infty}(2n-1)^2 a_n(t)\zeta^{2n-1}.$$

The time derivative of g is of course given by the time derivatives of the coefficients:

$$g_t(\zeta,t) = \sum_{n=0}^{\infty}\dot{a}_n(t)\zeta^{2n-1}.$$

To solve for the evolution of the coefficients $a_n(t)$ we truncate the series at N terms. The N fully implicit equations that we require will come from satisfying (44) at N equally spaced points

$$\zeta_j = \mathrm{e}^{\mathrm{i}\pi j/4N}, \qquad j = 0,\ldots,N-1,$$

which lie in the first quadrant on the unit circle.

To compute these implicit equations we first evaluate g, its derivatives, and subsequently v_n and κ, at each of the ζ_j. This is carried out very efficiently by using the inverse fast Fourier transform. Computing the complex analytic functions V and K from v_n and κ is simple in the space of their power series coefficients, for example

$$v_n = \sum_{n=-\infty}^{\infty} b_n\zeta^n \quad \Rightarrow \quad V = b_0 + \sum_{n=1}^{\infty} 2b_n\zeta^n,$$

(note that $b_n = \overline{b}_n$ by symmetry), so that the values of ζV_ζ in (44) are found by applying the fast Fourier transform to the values of v_n, manipulating the coefficients, and inverting the transform once more (a similar process holds for ζK_ζ). Now enforcing (44) at the ζ_j nodes furnishes us with N implicit equations for the time derivatives of the coefficients $\dot{a}(t)$. These are solved using a fully implicit time-stepping scheme (`ode15i` in `Matlab`) from a prescribed initial condition.

6.2. Scaled method

Since we are interested in the behaviour of bubbles near extinction, the above method can be improved by scaling space and time so that we more accurately compute the behaviour very close to the extinction time. To that end, we again let $\lambda(t)$ be the x-intercept of the bubble at time t, and define a new mapping function G and time-like variable T:

$$g(\zeta, t) = \lambda G(\zeta, T), \qquad T = -\log \lambda.$$

This is equivalent to the scaling we used in the derivation of the small bubble problem (26). The image of the unit circle under G is now the bubble shape scaled so that its x-intercepts are ± 1, and as $\lambda \to 0^+$, $T \to \infty$. We again write G as a power series

$$G(\zeta, T) = \sum_{n=0}^{\infty} A_n(T)\zeta^{2n-1}.$$

The area of the bubble is given by

$$\begin{aligned}\mathcal{A} = \frac{1}{2i}\oint_{\partial\Omega} \overline{z}\,\mathrm{d}z &= -\frac{\lambda^2}{2i}\oint_{|\zeta|=1} G(1/\zeta, T)G_\zeta(\zeta, T)\,\mathrm{d}\zeta \\ &= -\pi\lambda^2 \sum_{n=0}^{\infty} nA_n^2.\end{aligned}$$

From the constant rate of change of area (9) we therefore obtain

$$\dot{\lambda}\lambda = B(T)^{-1}, \qquad B(T) = \sum_{n=0}^{\infty} nA_n(A_n - A_n') \tag{45}$$

(here $'$ represents differentiation with respect to T). Armed with this relation we rewrite (44)

$$\mathrm{e}^{-T}(\Re\{(G - G_t)\overline{\zeta G_\zeta}\} + B) = B\Re\{\zeta\hat{V}_\zeta\} + \sigma\Re\{\zeta\hat{K}_\zeta\}, \quad |\zeta| = 1, \tag{46}$$

where $\hat{V}$ and $\hat{K}$ are the functions analytic in the unit disc such that

$$\Re\{\hat{V}\} = \frac{\Re\{(G - G_T)\overline{\zeta G_\zeta}\}}{|\zeta G_\zeta|}, \qquad \Re\{\hat{K}\} = \frac{\Re\{\zeta(\zeta G_\zeta)_\zeta\overline{\zeta G_\zeta}\}}{|\zeta G_\zeta|^3},$$

on $|\zeta| = 1$. This scheme is implemented numerically in a similar fashion to the last section, with one alteration. As we have not yet specified the scaling λ, and (45) is implied by (46) for any such scaling, we must replace one of the equations (say, at ζ_{N-1}) by a condition that fixes the scaling:

$$G(1, T) = 1.$$

Both the scaled and unscaled versions are very efficient due to their use of the fast Fourier transform. To produce the numerical results presented below we used $N = 128$ power series terms, which ran in the order of seconds on a modern desktop computer.

6.3. Numerical results

The numerical solution to the full problem (5)–(8) is used to verify the asymptotic predictions made from the small bubble problem; in particular we focus on the presence of an unstable steady state for values of σ in the critical range $\frac{1}{3} < \sigma < \frac{1}{2}$, and the stability of the two trivial steady states, the circle and the slit.

In Figure 9 we plot the numerical solutions for two initially elliptical bubbles with nearly identical aspect ratios, for a surface tension value $\sigma = 0.3757$ within the critical range. We compare both the unscaled and scaled versions of our numerical scheme. The unscaled method shows the bubbles shrinking to a point, but before the small bubble limit is approached the two solutions look very similar, and we cannot examine the behaviour very close to the point of extinction. In the scaled version, we see that the bubble quickly tends toward the nontrivial (unstable) bubble shape in the stretched time variable T, but then eventually heads toward either the circle or slit, the outcome due purely to the slight difference in initial condition. While it is technically possible that an initial condition may be just such that the bubble tends to the bubble shape represented by the nontrivial steady state exactly, in general bubbles will contract as either circular or slit-type bubble shapes.

7. Discussion

We have performed an analytic and numerical investigation of the effects of surface tension and kinetic undercooling on the shape of a contracting bubble in a Hele–Shaw cell. As the bubble shrinks to a point in the limit $t \to t_f^-$, it asymptotically approaches a shape corresponding to a steady state of the leading order small bubble approximation (26). This approximation has two "trivial" steady states whose stability depends on the value of the nondimensional surface tension parameter $\sigma = \hat{\sigma}/(\hat{c}\hat{Q})$: the circle, which is stable for $\sigma > \frac{1}{3}$, and the infinitely thin slit, which is stable for $\sigma < \frac{1}{2}$. For surface tension values in the critical range $\frac{1}{3} < \sigma < \frac{1}{2}$, where both trivial steady states are stable, we found a third, unstable branch of steady states, on which the bubble shape has an aspect ratio lying between zero and one. Our numerical solution of the full Hele–Shaw problem shows that, while bubbles may initially evolve toward this unstable bubble shape, very close to the point of extinction they chang their trajectory and evolve to either a circle or slit, in agreement with the stability analysis. There are, however, many unresolved problems and areas for further study, some of which we outline below.

7.1. Bubble break-up

The focus of our study is on the asymptotic shape of a single bubble very close to extinction. For simplicity we have only considered symmetric bubbles that remain connected up to the time of extinction; this avoids the question of the breakup of a single bubble into multiple disconnected ones, which may happen for concave initial conditions (for instance, initially "dumbell" shaped bubbles). In this case, more sophisticated

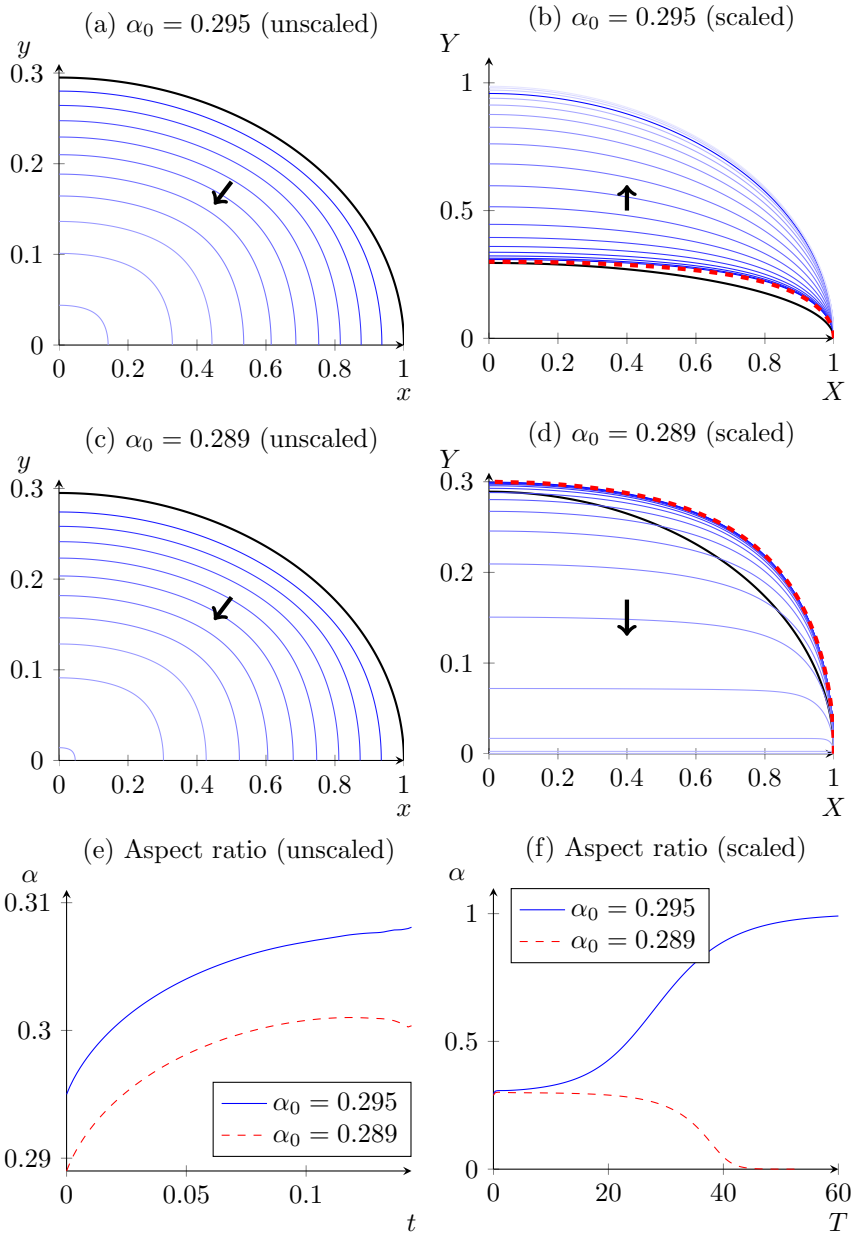

Figure 9. The evolution of the shape of two initially elliptical bubbles (depicted by the thick solid line) of aspect ratios of ratios $\alpha_0 = 0.295$ and $\alpha_0 = 0.289$, computed using the two numerical methods discussed in Section 6. The unscaled method (left) shows the evolution of the bubbles while their sizes are $\mathcal{O}(1)$; the two solutions do not appear to differ greatly at this scale. The scaled method (right), where lengths have been scaled by the interface's x-intercept λ, and $T = -\log\lambda$ is the stretched time variable, is useful for calculating how the bubbles behave very close to extinction. We see both bubbles initially tend toward the (unstable) steady state as described in Section 5 for the given value of σ (shown as a broken line), but ultimately tend toward either (b) a circle, or (d) a slit, both of which are stable according to the results in Section 4.

numerical techniques are required than those described in this paper, since our scheme is based on a conformal mapping from the unit disc, and therefore requires the fluid region to be simply connected.

Additionally, the rescaled problem (23) in Section 3 is no longer valid when there are multiple bubbles. While it is reasonable to expect each bubble to behave qualitatively like the solution to (23) when it nears extinction, there is no simple formula for the exact rate of decrease in the area of each bubble. The rate of decrease of area over all bubbles is -2π, while each individual bubble will be shrinking at a lesser rate, meaning surface tension will be more dominant, and circular extinction behaviour more likely. If, however, a point in time is reached where all bubbles except one has become extinct, the limiting behaviour of the remaining bubble will again be described by (23).

7.2. Pure kinetic undercooling ($\sigma = 0$)

We have not examined in depth the problem of pure kinetic undercooling (that is, when $\sigma = 0$). In this case, experiments with our full numerical scheme suggest the formation of corners in finite time, for both contracting (t decreasing) and expanding (t increasing) bubbles. Interfaces with corners are allowable (weak) solutions in the absence of surface tension, as kinetic undercooling acts on the velocity, rather than the curvature, of the interface [37, 9]. Setting $\sigma = 0$ in the small bubble problem (26) reduces it to a local, though nonlinear and singular first order partial differential equation

$$\sqrt{\xi^2 + (1-\xi^2)F_\xi^2} = \xi F + (1-\xi)^2 F_\xi - \xi F_T, \quad F(0,T) = 0,$$

(note that $P(T) = 1$). An example numerical solution is included in Figure 10, showing the possible development of a corner on the x-axis. An exact solution may be able to be constructed that could shed light into the formation of such finite-time corners. Trivially, we note that a (weak) solution is the rectangular bubble represented by $F(\xi, T) = \alpha(T)$, where α satisfies

$$1 = \alpha - \frac{\mathrm{d}\alpha}{\mathrm{d}T} \;\Rightarrow\; \alpha = 1 - k\mathrm{e}^T,$$

(where k is a constant). Recalling that $T = -\log\lambda$, where λ is the x-intercept of the bubble boundary, the fact that α goes to zero for a finite value of T implies that the bubble does not become arbitrarily small in the x-direction, but rather tends to a line of finite length on the x-axis. This behaviour may be generic for solutions to the full problem that form corners on the x-axis.

7.3. Higher mode instabilities and other steady states

Additionally, our analysis has focused on the instability of bubbles with an initially nonzero second mode perturbation (ellipses, for example). This focus is motivated by the stability analysis in Section 4, where we observe that the second mode is the most unstable. However, if the second mode is initially zero (which will be true, for instance, for a bubble of n-fold symmetry, where $n > 2$), it will be identically zero for all time.

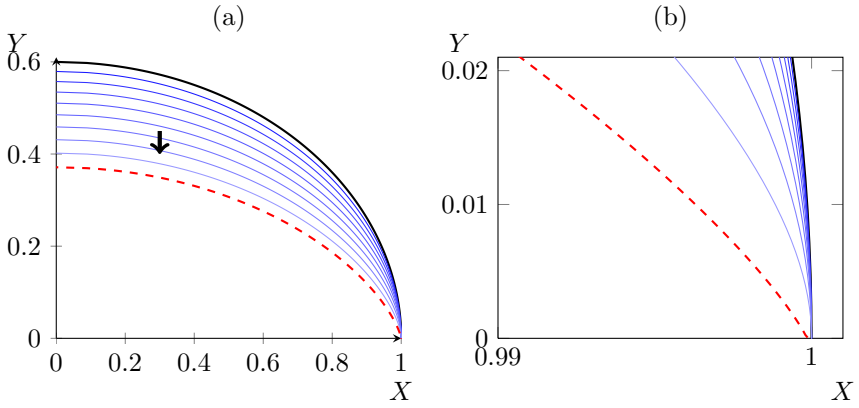

Figure 10. A numerical solution to the small bubble approximation (26) in the phyiscal coordinate X, for pure kinetic undercooling ($\sigma = 0$). An initially elliptical bubble (represented by the thick solid line) appears to evolve to a curve with a corner on the x-axis (represented by the thick broken line). The numerical scheme does not continue past the point at which the corner develops.

In theses special cases, the shrinking circular bubble will have a bifurcation point (less than $\frac{1}{3}$), depending on n, given by (21). For surface tension values less than this bifurcation point, the circle is unstable, but the bubble cannot shrink to a slit due to its symmetry; instead, the bubble will tend towards an analogous n-fold symmetric self-similar solution, which likely approaches a regular polygon of the same symmetry (similar solutions are discussed in [29, 34] for shear-thickening fluid in the absence of nonlinear boundary effects, and in the focusing problem for the porous medium equation; see [34], p. 10, 14).

To take an example, for a bubble with four-fold symmetry the bifurcation point for the circle according to (21) is $\sigma = 1/15 = 0.066\ldots$. In Figure 11 we show numerical solutions computed by the methods outlined in Section 6 for an initially four-fold symmetric bubble. The solution behaviour demonstrates the bifurcation in the stability of the circle, with the bubble heading toward a circle for $\sigma = 0.07$ and toward another steady state, possibly a sharp-cornered square diamond, for $\sigma = 0.04$. In our small bubble approximation (26), the diamond could be considered the (weak) steady state solution $F = 1 - X = 1 - \sqrt{1 - \xi^2}$. We note that special care must be taken in the numerical scheme to ensure the second mode does not become nonzero due to numerical error. Otherwise, the instability quickly takes over and the bubble ceases to by symmetric, tending eventually to slit-type extinction.

7.4. Stability of the nontrivial branch

The instability of the nontrivial steady state was shown numerically (see Figure 7). A proper stability analysis would require the determination of the eigenvalues μ of the linearisation of (26) about the nontrivial steady state. If we write $F = F_0(\xi) + \epsilon F_1(\xi, T)$, where F_0 is the steady state solution and F_1 is the linear correction term, the eigenvalue

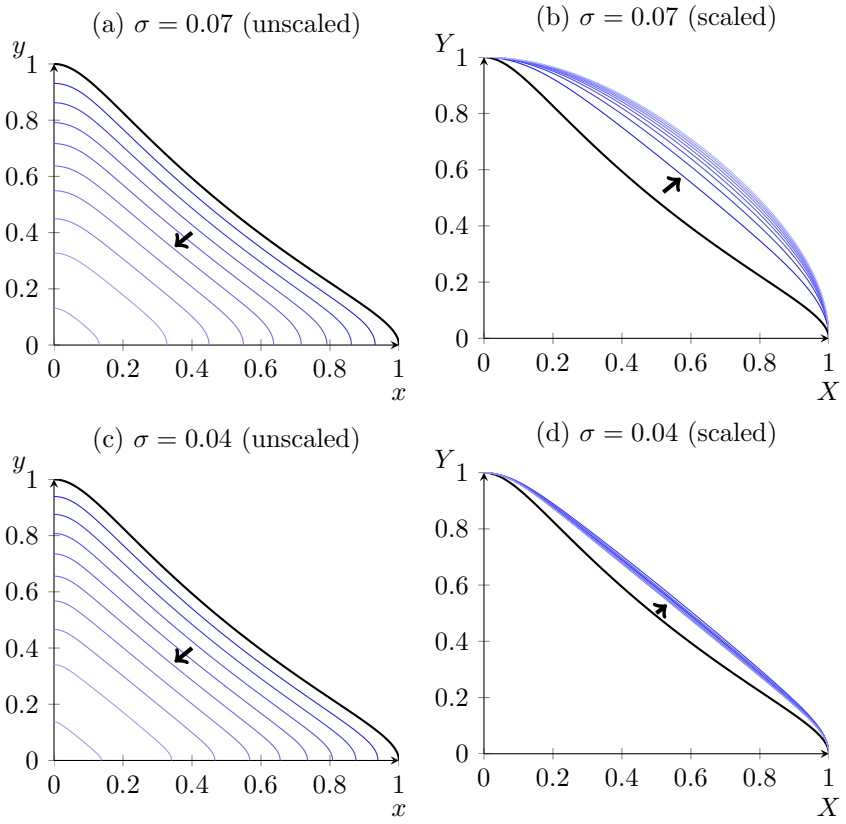

Figure 11. An example of a shrinking four-fold symmetric bubble, using the numerical methods from Section 6, with initial condition indicated by the thick solid line. According to (21), the critical value of the surface tension for the fourth mode is $\sigma = 1/15 = 0.066\ldots$. For $\sigma = 0.07$ (top) the bubble tends to a (stable) circle, while for $\sigma = 0.04$ (bottom) the bubble appears to tend toward a (unstable) square diamond.

problem is of the form

$$M_0(\xi)(1-\mu)G + M_1(\xi)G' + M_2(\xi)G'' \\ = M_4(\xi)(2-\mu)\int_0^1 G(\xi')\frac{\xi'}{\sqrt{1-\xi'^2}}\,\mathrm{d}\xi' + CG'(0),$$

where $F_1 = \mathrm{e}^{\mu T}G(\xi)$. The coefficients M_k and C depend on the nontrivial steady state, which can only be computed numerically for a given value of σ. Furthermore, the integral on the right hand side makes the problem nonlocal. Similar nonlocal eigenvalue problems have been studied in the context of reaction-diffusion equations [43, 44]. It is possible that similar methods may be used in the present example. From our numerical results, we expect that there will be at least one positive eigenvalue, with some bubbles initially heading toward the nontrivial steady state, but eventually heading toward either a circle or slit. We leave these issues for further research.

References

[1] H.S. Hele–Shaw. The flow of water. *Nature*, 58(1489):33–36, 1898.

[2] S.D. Howison. Bibliography of free and moving boundary problems in Hele–shaw and Stokes flow, August 1998. `http://people.maths.ox.ac.uk/howison/Hele-Shaw/`.

[3] B. Gustafsson and A. Vasil'ev. *Conformal and potential analysis in Hele-Shaw cells.* Birkhäuser-Verlag, 2006.

[4] P.G. Saffman and G.I. Taylor. The penetration of a fluid into a porous medium or Hele-Shaw cell containing a more viscous liquid. *Proc. R. Soc. Lond. A*, 245:312–329, 1958.

[5] E. Dibenedetto and A. Friedman. The ill-posed Hele–Shaw model and the Stefan problem for supercooled water. *Trans. Amer. Math. Soc.*, 282:183–204, 1984.

[6] S.D. Howison. Complex variable methods in Hele–Shaw moving boundary problems. *Eur. J. Appl. Math.*, 3:209–224, 1992.

[7] S.D. Howison. Fingering in Hele–Shaw cells. *J. Fluid Mech.*, 167:439–453, 1986.

[8] S.D. Howison. Bubble growth in porous media and Hele–Shaw cells. *Proc. Roy. Soc. Edin. A*, 102:141–148, 1986.

[9] J. R. King, A. A. Lacey, and J. L. Vazquez. Persistence of corners in free boundaries in Hele–Shaw. *Eur. J. Appl. Math.*, 6:455–490, 1995.

[10] H.D. Ceniceros and T.Y. Hou. Convergence of a non-stiff boundary integral method for interfacial flows with surface tension. *Math. Comput.*, 67:137–182, 1998.

[11] T.Y. Hou, J.S. Lowengrub, and M.J. Shelley. Removing the stiffness from interfacial flow with surface tension. *J. Comp. Phys.*, 114:312–338, 1994.

[12] L.P. Kadanoff. Exact solutions for the Saffman–Taylor problem with surface tension. *Phys. Rev. Lett.*, 65:2986–2988, 1990.

[13] E.D. Kelly and E.J. Hinch. Numerical simulations of sink flow in the Hele–Shaw cell with small surface tension. *Eur. J. Appl. Math.*, 8:533–550, 1997.

[14] J.R. King and J.D. Evans. Regularization by kinetic undercooling of blow-up in the ill-posed Stefan problem. *SIAM J. Appl. Math.*, 65:1677–1707, 2005.

[15] A. Fasano, G.H. Meyer, and M. Primicerio. On a problem in the polymer industry: theoretical and numerical investigation of swelling. *SIAM J. Math. Anal.*, 17:945–960, 1986.

[16] D.S. Cohen and T. Erneux. Free boundary problems in controlled release pharmaceuticals. I: Diffusion in glassy polymers. *SIAM J. Appl. Math.*, 48:1451–1465, 1988.

[17] S.W. McCue, M. Hsieh, T.J. Moroney, and M.I. Nelson. Asymptotic and numerical results for a model of solvent-dependent drug diffusion through polymeric spheres. *SIAM J. Appl. Math.*, 71:2287–2311, 2011.

[18] J.S. Langer. Instabilities and pattern formation in crystal growth. *Rev. Mod. Phys.*, 52:1–28, 1980.

[19] L.A. Romero. *The fingering problem in a Hele–Shaw cell.* PhD thesis, California Institute of Technology, 1981.

[20] U. Ebert, B.J. Meulenbroek, and L. Schäfer. Convective stabilization of a Laplacian moving boundary problem with kinetic undercooling. *SIAM J. Appl. Math.*, 68:292–310, 2007.

[21] U. Ebert, F. Brau, G. Derks, W. Hundsdorfer, C-Y. Kao, C. Li, A. Luque, B. Meulenbroek, S. Nijdam, V. Ratushnaya, L. Schäfer, and S. Tanveer. Multiple scales in streamer discharges, with an emphasis on moving boundary approximations. *Nonlinearity*, 24:C1–C26, 2011.

[22] C.-Y. Kao, F. Brau, U. Ebert, L. Schäfer, and S. Tanveer. A moving boundary model motivated by electric breakdown: Ii. initial value problem. *Physica D*, 239:1542–1559, 2010.

[23] A. Luque, F. Brau, and U. Ebert. Saffman–Taylor streamers: Mutual finger interaction in spark formation. *Phys. Rev. E*, 78:016206, 2008.

[24] Y-T. Kim, N. Goldenfield, and J. Dantzig. Computation of dendritic microstructures using a level set method. *Phys. Rev. E*, 62:2471–2474, 2000.

[25] Z. Li and B. Soni. Fast and accurate numerical approaches for Stefan problems and crystal growth. *Numer. Heat Tr. B-Fund.*, 35:461–484, 1999.

[26] F. Gibou, R. Fedkiw, R. Caflisch, and S. Osher. A level set approach for the numerical simulation of dendritic growth. *J. Sci. Comp.*, 19:183–199, 2003.

[27] V. Entov and P. Etingof. On the breakup of air bubbles in a Hele–Shaw cell. *Eur. J. Appl. Math.*, 22:125–149, 2011.

[28] S-Y. Lee, E. Bettelheim, and P. Weigmann. Bubble break-off in Hele–Shaw flows—singularities and integrable structures. *Physica D*, 219:22–34, 2006.

[29] J.R. King and S.W. McCue. Quadrature domains and p-Laplacian growth. *Complex Anal. Oper. Th.*, 3:453–469, 2009.

[30] V.M. Entov and P.I. Etingof. Bubble contraction in Hele–Shaw cells. *Q. J. Mech. Appl. Math.*, 44:507–535, 1991.

[31] S.W. McCue, J.R. King, and D.S. Riley. Extinction behaviour of contracting bubbles in porous media. *Q. J. Mech. Appl. Math.*, 56:455–482, 2003.

[32] S.D. Howison. Cusp development in Hele–Shaw flow with a free surface. *SIAM J. Appl. Math.*, 46:20–26, 1986.

[33] M.C. Dallaston and S.W. McCue. New exact solutions for Hele–Shaw flow in doubly connected regions. *Phys. Fluids*, 24:052101, 2012.

[34] S.W. McCue and J.R. King. Contracting bubbles in Hele–Shaw cells with a power-law fluid. *Nonlinearity*, 24:613–641, 2011.

[35] Yu.E. Hohlov and M. Reissig. On classical solvability for the Hele–Shaw moving boundary problems with kinetic undercooling regularization. *Eur. J. Appl. Math.*, 6:421–439, 1995.

[36] M. Reissig, D. V. Rogosin, and F. Hübner. Analytical and numerical treatment of a complex model for Hele–Shaw moving boundary value problems with kinetic undercooling regularization. *Eur. J. Appl. Math.*, 10:561–579, 1999.

[37] S.J. Chapman and J.R. King. The selection of Saffman–Taylor fingers by kinetic undercooling. *J. Eng. Math.*, 46:1–32, 2003.

[38] L. Paterson. Radial fingering in a Hele–Shaw cell. *J. Fluid Mech.*, 113:513–529, 1981.

[39] M.A. Grayson. The heat equation shrinks embedded plane curves to round points. *J. Differ. Geom.*, 26:285–314, 1987.

[40] S.B. Angenent. Shrinking doughnuts. In N.G. Lloyd, W.M. Ni, L.A. Peletier, and J. Serrin, editors, *Nonlinear Diffusion Equations and their Equilibrium States*. Birkhäuser, 1992.

[41] J.R. King. Emerging areas of mathematical modelling. *Phil. Trans. R. Soc. Lond. A*, 358:3–19, 2000.

[42] C.L. Farmer and S.D. Howison. The motion of a viscous filament in a porous medium or Hele-Shaw cell: a physical realisation of the Cauchy–Riemann equations. *Appl. Math. Lett.*, 19:356–361, 2006.

[43] P. Freitas. A nonlocal Sturm–Liouville eigenvalue problem. *Proc. R. Soc. Edin. A*, 124:169–188, 1994.

[44] D. Iron and M.J. Ward. A metastable spike solution for a nonlocal reaction-diffsuion model. *SIAM J. Appl. Math.*, 60:778–802, 2000.